ELSEVIER

Contents lists available at ScienceDirect

Corrosion Science

journal homepage: www.elsevier.com/locate/corsci





Local pH and oxygen concentration at the interface of Zn alloys in Tris-HCl or HEPES buffered Hanks' balanced salt solution

Cheng Wang ^{a,*}, Xiao Liu ^b, Di Mei ^{a,c}, Min Deng ^a, Yufeng Zheng ^b, Mikhail L. Zheludkevich ^{a,d}, Sviatlana V. Lamaka ^a

- ^a Institute of Surface Science, Helmholtz-Zentrum Hereon, Geesthacht 21502, Germany
- ^b School of Materials Science and Engineering, Peking University, Beijing 100871, China
- ^c School of Materials Science and Engineering & Henan Key Laboratory of Advanced Magnesium Alloy, Zhengzhou University, Zhengzhou 450001, China
- ^d Institute for Materials Science, Faculty of Engineering, Kiel University, Kiel 24103, Germany

ARTICLE INFO

Keywords: Local pH Local oxygen concentration Tris-HCl HEPES Biodegradable Zn-based alloy Hanks' balanced salt solution

ABSTRACT

Although Tris-HCl and HEPES are typically used pH buffers for in vitro studies, they are recently proven to be unable to stabilize local pH at Mg interface in simulated body fluids. In this study, local pH close to physiological (7.1–7.5) was found at metal/fluid interface of pure Zn, Zn-0.8 wt%Ca and Zn-0.8 wt%Mg alloys in Tris-HCl or HEPES buffered Hanks' balanced salt solution (HBSS) at 37 °C under hydrodynamic conditions. High rate oxygen consumption was detected above Zn alloys in various HBSS electrolytes. These findings support the previous recommendation of using synthetic pH buffers for in vitro studies of biodegradable Zn-based alloys.

1. Introduction

Zinc, as an essential trace element in the human body, has enabled Zn-based alloys to be considered as an emerging alternative biodegradable metal. Their superior mechanical properties and suitable degradation rates not only satisfy the clinical requirements of biodegradable metals, but also facilitate the potential applications in bone repair and cardiovascular intervention [1–5]. Therefore, multiple research groups have reported on optimizing alloy design of biodegradable Zn for load-bearing applications [6–9].

Up to date, an increasing number of studies disclosed the biodegradable behavior of Zn and its alloys under in vitro/ in vivo conditions [7,10–14]. Various electrolytes such as 0.9 wt% NaCl solution [15], Ringer's solution [16], phosphate buffered saline (PBS) [17], Hanks' balanced salt solution (HBSS) [18], and simulated body fluid (SBF) [19] have been selected as the empirical in vitro test media benefited from the previous experience on the biodegradable investigations of Mg and Fe. Besides the synergistic influences induced by inorganic ions [20,21], organic molecules [22,23], proteins [24,25], cells [26], temperature, partial pressure and concentration of the dissolved oxygen, pH of tissue fluid is of great importance in the physiological environment where a broad fluctuation of acid-base balance may cause protein denaturalization and cell apoptosis [27]. Thus, executing in vitro experiments on

Zn alloys in a suitable medium with a specific pH range (e.g. 7.35–7.45 for blood plasma) would be beneficial to the evaluation of the corrosion performance and the elucidation of the degradation mechanism. Meanwhile, corrosion, involving oxidation and reduction, often leads to acidification at local anodes caused by the hydrolysis of dissolved metal cations and alkalization at local cathodes caused by OH generation as a result of the reduction of water or oxygen [28].

The pH level of blood plasma or interstitial fluid is naturally controlled by the inherent buffer system mainly containing phosphate $\rm H_2PO_4/HPO_4^{2-}$ and carbonate $\rm CO_2/HCO_3^-/H_2CO_3$ pH buffers [29]. Amino acids of proteins also possess pH buffering capacity [24]. In order to simulate the inherent buffer system, a $\rm HCO_3^-/H_2CO_3$ buffer couple has been established through cooperation between a certain amount of NaHCO_3 (2.2 g/L) and a controlled CO_2 atmosphere (5%) [30]. It has been reported that the degradation rates of pure Mg and its alloys in NaHCO_3 buffered Earle's balanced salt solution (EBSS) were comparable to in vivo results [31]. Similarly, gaseous CO_2 buffered HBSS was capable of predicting in vivo degradation rate of Mg alloy [32]. Yet, NaHCO_3/CO_2 buffer found only limited application owing to rather high requirements for apparatus and operations.

As an alternative for controlling pH during in vitro studies, several synthetic pH buffers are used for preparing corresponding test media. Tris(hydroxymethyl) aminomethane buffer with HCl (Tris-HCl) and 4-

E-mail address: cheng.wang@hereon.de (C. Wang).

^{*} Corresponding author.

(2-hydroxyethyl)— 1-piperazineethanesulfonic acid (HEPES) have been considered as favorable candidates although they cannot be traced inside the human body [33,34]. The buffer capacities of HEPES and Tris-HCl are atmosphere-independent, leading to an experimental convenience to some extent. Tris-HCl buffer maintains pH in the range from 7.1 to 9.1. The principle of pH buffering is that the bonded H^+ in Tris-HCl consumes the OH generated in the course of cathodic reaction during anodic metal dissolution, while the amino-group of Tris depletes the H^+ ions provided by the hydrolysis of metal ions [35]. HEPES is a zwitterion buffer covering a pH range (6.8–8.2) widely used in the cell culture medium, where it neutralizes excessive protons to inhibit acidification [34,36].

Even though the pH buffer system plays a crucial role in keeping the bulk electrolyte in a determined pH range, doubts remain whether it is effective for stabilizing local pH at the metal/liquid interface due to the strong ionic gradients there. Moreover, local pH at the interface is one of the substantial factors during metal degradation. Recently, with the assistance of scanning ion electrode technique (SIET), Tris-HCl was shown to be unable to buffer the local pH above Mg surface despite the fact the bulk pH of the electrolyte was under control [20]. The Ca²⁺/Mg²⁺-binding effect of Tris and the increased quantities of Cl⁻ ions from HCl alter the degradation behavior and accelerate the degradation rate. Likewise, HEPES in HBSS could not stabilize the values of local pH [37,38] and HEPES in EBSS was shown to retard the precipitation of insoluble Ca-P-carbonate layer during the degradation of Mg, strongly affecting the degradation kinetics [39].

Currently, the interaction between synthetic pH buffers and Zn has been put on the agenda. Tris-HCl buffer was recommended as an optimum buffer system for in vitro research on the degradation behavior of Zn and its alloys [23,40]. In spite of the fact that the degradation rate of Zn and its alloys in Tris-HCl buffered SBF increases, it approaches in vivo degradation rate. Yet it remains unclear whether Tris-HCl succeeds in stabilizing the local pH above the surface that determines the biodegradation behavior of Zn and its alloys. Although the Ca²⁺-binding effect of Tris could resemble the role of albumin [24], it suppresses the formation of Ca-P-containing products layer, which has been reported as a significant factor because it provides partial corrosion protection property for biodegradable Mg and Fe [41,42]. The role of Ca-P-containing products during the biodegradation of Zn deserves to be explored.

This study aims at exploring the pH buffering effect of Tris-HCl and HEPES on the degradation of pure Zn and Zn-based alloys in a pseudophysiological environment from the viewpoint of local electrochemistry, providing additional information for future in vitro/vivo studies of biodegradable Zn-based materials. A detailed study on the evolution of the local pH of the electrolyte adjacent to the surface of Zn-based materials in HBSS with or without the addition of Tris-HCl and HEPES was performed. The concentration of dissolved oxygen (DO) was simultaneously recorded to explore the impact of Tris-HCl and HEPES on the degradation behavior and protective properties of formed corrosion products, since oxygen reduction reaction (ORR) is considered the major cathodic reaction during Zn degradation.

2. Experimental

Extruded pure Zn (99.99% purity), Zn-0.8 wt%Mg (Zn-0.8Mg), and Zn-0.8 wt%Ca (Zn-0.8Ca) rods (10 mm in diameter) were machined into the rod shape ($\Phi=2$ mm) and embedded in the epoxy resin with a round face exposed as a working electrode (Fig. 1). The specimens were ground successively using SiC papers from 1200 grit to 4000 grit and then cleaned in deionized water and absolute ethanol. The elemental composition of Zn alloys has been reported elsewhere [6]. The components of all the electrolytes used in this work are summarized in Table 1. There are six different electrolytes: Ca²⁺-free HBSS (hereafter denoted as HBSS), Tris-HCl buffered Ca²⁺-free HBSS (hereafter denoted as HBSS+Tris-HCl), HEPES buffered Ca²⁺-free HBSS (hereafter denoted as HBSS+HEPES), Ca²⁺-containing HBSS (hereafter denoted as

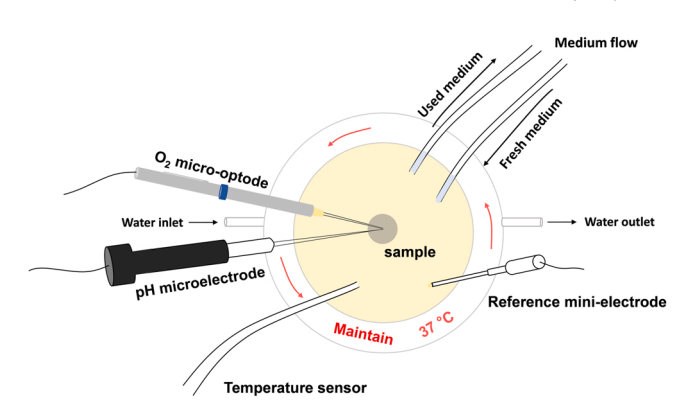


Fig. 1. A schematic of the setup (top view) for the simultaneous measurement of local pH and oxygen concentration above the specimen of Zn-based alloys at $37~^{\circ}$ C under hydrodynamic conditions.

Table 1The composition and corresponding abbreviation of HBSS electrolytes used in this study.

Components	Concentration / mM					
	Ca ²⁺ - free	Tris- HCl	HEPES	Ca ²⁺	Ca ²⁺ +Tris- HCl	Ca ²⁺ +HEPES
KCl				5.33		
KH ₂ PO ₄				0.44		
NaHCO ₃				4.17		
NaCl				137.9		
D-Glucose				5.56		
Na ₂ HPO ₄				0.34		
CaCl ₂	_	_	_		1.26	
MgCl ₂ .6H ₂ O	_	_	_		0.49	
MgSO ₄ .7H ₂ O	_	_	_		0.41	
Tris-HCl	_	50.5	_	_	50.5	-
HEPES	_	_	25.0	_	_	25.0
pH _{initial}				7.40		

 ${\rm Ca^{2+}HBSS}$), Tris-HCl buffered ${\rm Ca^{2+}}$ -containing HBSS (hereafter denoted as ${\rm Ca^{2+}HBSS+Tris-HCl}$), HEPES buffered ${\rm Ca^{2+}}$ -containing HBSS (hereafter denoted as ${\rm Ca^{2+}HBSS+HEPES}$).

Local pH was recorded by a commercial glass-type pH microelectrode with a tip diameter of 10 µm (Unisense, pH-10), together with a mini Ag/AgCl reference electrode. Local O2 concentration was monitored using a needle-type retractable fiber-optic O₂ micro-optode (OXR50-UHS) with a tip diameter of 50 µm coupled with a Fire-StingO2 oxygen logging meter, both from PyroscienceTM. Both pH microelectrode and DO micro-optode were integrated into a commercial SVET-SIET system (Applicable ElectronicsTM) for probe movement. The data was acquired by LV4 software from SciencewaresTM in parallel with PyroOxygenLogger from Pyroscience™. Both pH microelectrode and O₂ micro-optode were positioned at 50 µm above the sample surface using a custom-made dual-head stage for in situ simultaneous monitoring of local pH and O₂ concentration. The distance between pH microelectrode and O2 micro-optode was kept at 50 µm in horizontal planes via micromanipulators. Local H2 concentration was measured using a H2 microsensor (10 µm tip diameter, Unisense).

Fig. 1 exhibits a schematic of the setup for the simultaneous measurement of local pH and oxygen concentration at the interface of Zn-based alloys in various HBSS electrolytes at 37 °C under hydrodynamic conditions. For characterizing the distribution of the local pH and DO concentration above the metal surface, a series of sample-centered areas (3000 $\mu m \times 3000~\mu m$) was successively scanned with the rate of 100 μm per step in order to follow the local progression. The sampling interval in each step was 3 s and the total time for one map (31 \times 31 grid) was approximately 1 h counting the time for moving the microelectrodes. The 3 s sampling interval was sufficient since the pH gradient

between two consecutive measuring points was less than one pH unit in this work. The measurements were conducted at 37 $^{\circ}C$ under the hydrodynamic condition with a flow rate of 1.0 mL min $^{-1}$ controlled by a peristaltic pump (Medorex). The volume of the cell for local measurements was 5 mL, so that the medium was fully renewed every 5 min. The used medium was thrown to waste and not recirculated. A similar measurement of local concentration of $\rm H_2$ and $\rm O_2$ was performed to investigate the cathodic reactions during the degradation of Zn-based alloys in $\rm Ca^{2+}HBSS$.

Electrochemical impedance spectra (EIS) were measured by a Gamry Interface 1010 potentiostat/galvanostat with a typical three-electrode configuration: a working electrode (with an exposed area of 0.5 cm²), a saturated Ag/AgCl reference electrode, and a counter electrode (a platinum wire coil). EIS measurements were continually executed at open circuit potential for all the Zn-based alloys in different HBSS electrolytes at 37 $^{\circ}$ C up to 24 h of immersion. The amplitude of 10 mV RMS sinusoidal perturbation over a frequency range from 100 kHz to 0.1 Hz was applied. The volume of the electrolyte was 400 mL. The electrolyte was constantly stirred at a rate of 250 rpm.

The weight loss of all three Zn alloys was measured three times after immersing the samples in either of six HBSS electrolytes (Table 1) at 37 °C under hydrodynamic conditions. The medium in a 500 mL cell was constantly refreshed by a peristaltic pump at a rate of 0.2 mL min $^{-1}$. After 3 days of immersion, the specimens were cleaned using chromic acid (200 g/L) to remove the corrosion products from the surface. The specimens were then rinsed with deionized water, dried in the air, and weighed using the analytical balance. The corrosion rates were calculated from the weight loss based on the equation: $CR=10~\Delta m~\rho^{-1}~A^{-1}~t^{-1}$. CR is the corrosion rate in mm y $^{-1}$, Δm is the weight loss (g), ρ is the material density (g cm $^{-3}$), A is the initial surface area of the specimen (cm 2), and t is the immersion time (year).

3. Results and discussions

3.1. The degradation behavior of pure Zn in HBSS containing different pH buffers at 37 $^{\circ}$ C under hydrodynamic conditions

The visual appearance and the distribution of local pH and DO concentration of pure Zn, Zn-0.8Mg, and Zn-0.8Ca in different HBSS electrolytes at 37 $^{\circ}$ C under hydrodynamic conditions are shown in Figs. 2–4, respectively.

For pure Zn (Fig. 2), in HBSS without any synthetic buffers, an active anodic site appeared within 1-hour immersion as indicated by the acidified region in the local pH distribution. Local pH decreased from 7.40 to 5.84 at the anodic site due to the hydrolysis reaction of Zn^{2+} ions, generating H^+ ions causing slight acidification (Eq. 1) [43].

$$Zn^{2+} + 2H_2O \rightarrow Zn(OH)_2 + 2H^+ \quad pK_{hvd} = 8.96$$
 (1)

In the meantime, near the active pit, a cathodic site was found with higher local pH (max. 8.66) compared to the bulk pH (7.40). The simultaneous measurement of local DO concentration gave direct support to the ORR (Eq. 2) occurring above the major area of the surface outside the acidified anodic site.

$$O_2 + 4e^- + 2H_2O \rightarrow 4OH^-$$
 (2)

Stable development of pitting corrosion was exhibited on pure Zn with immersion time as demonstrated by the remaining active anodic sites after 12 h of immersion in HBSS. The lowest pH at the anodic site remained below 6.00. According to the simulation of Hydra-Medusa (Fig. 6(a)), it was difficult to generate corrosion products in the pit for passivating it at this low pH. ORR occurred at the cathodic site around the pit that produced hydroxyls, leading to an increase of local pH and consequently inducing the precipitation of corrosion products around the pits as seen in the optical image. The formation of corrosion products

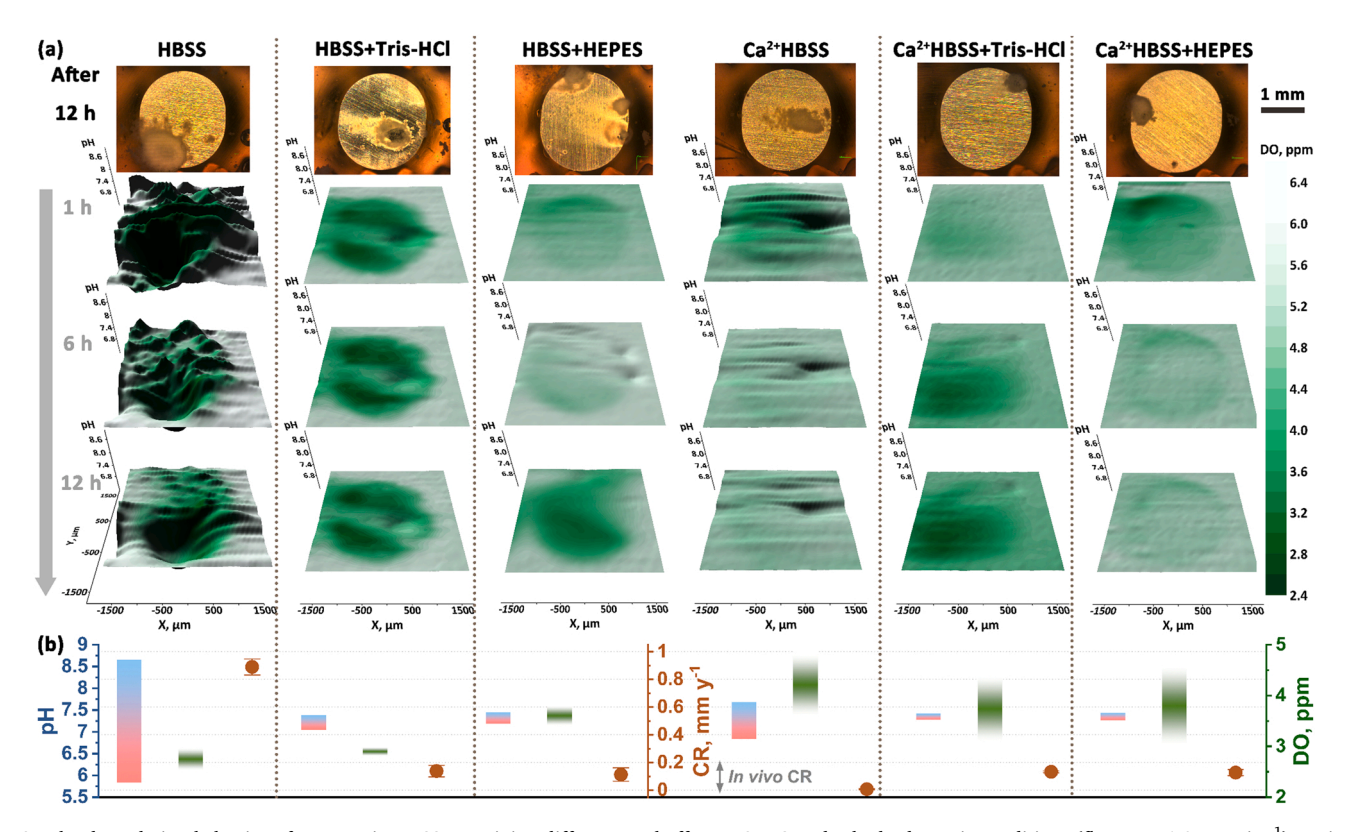


Fig. 2. The degradation behavior of pure Zn in HBSS containing different pH buffers at 37 °C under hydrodynamic conditions (flow rate 1.0 mL min⁻¹). a visual appearance after 12 h of immersion, distribution of local pH (3D topography), and DO concentration (green color code) above the metal surface with immersion time. b a summary of local pH value (red-blue gradient), the range of the minimum concentration of dissolved oxygen (green) and the corrosion rates, an average of three measurements (brown filled circles).

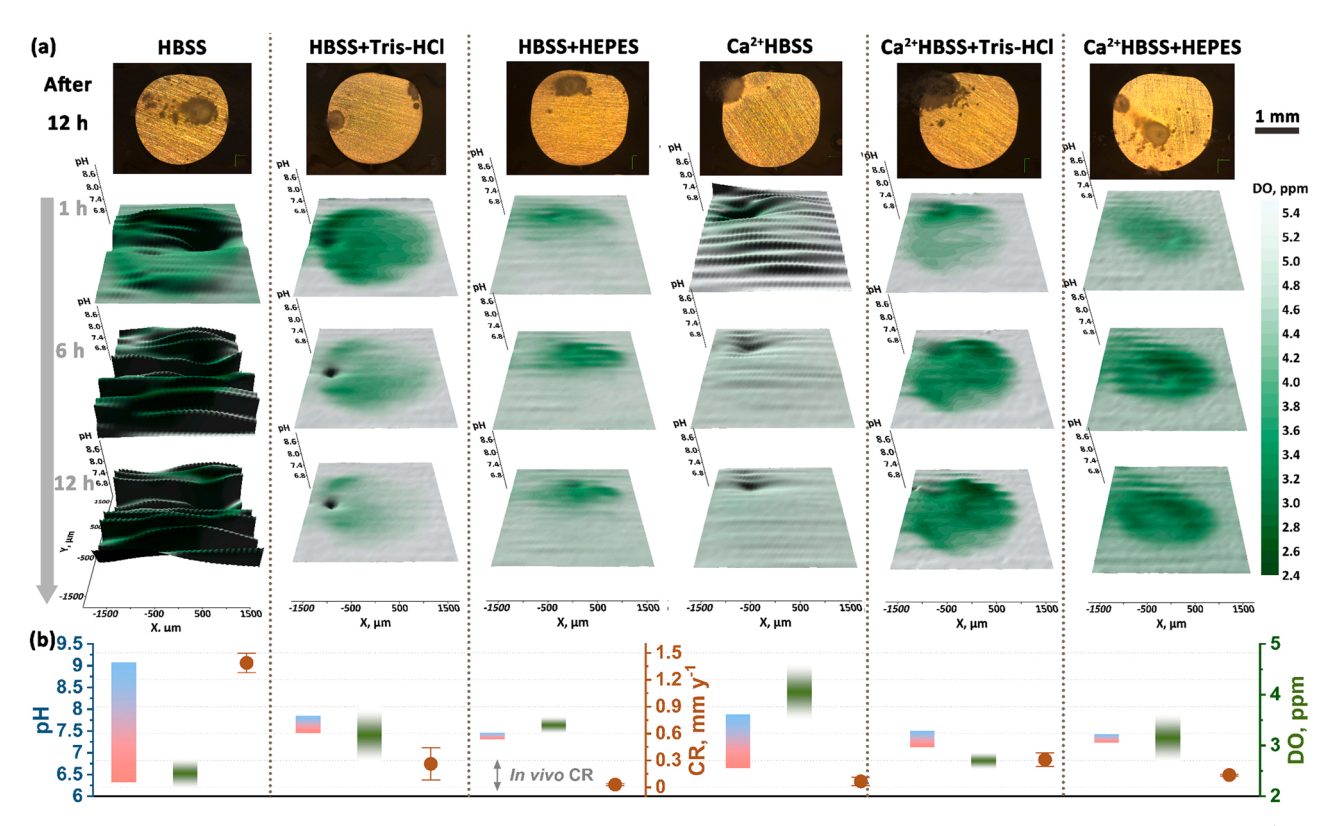


Fig. 3. The degradation behavior of Zn-0.8Mg in HBSS containing different pH buffers at 37 °C under hydrodynamic conditions (flow rate 1.0 mL min⁻¹). a visual appearances after 12 h of immersion, distribution of local pH (3D topography), and DO concentration (green color code) above the metal surface with immersion time. b a summary of local pH value (red-blue gradient), the range of minimum concentration of dissolved oxygen (green) and the corrosion rates, an average of three measurements (brown filled circles).

above the pit blocked the diffusion of oxygen, intensifying the acidification in the pit. For maintaining electric neutrality, chloride ions kept infiltrating the dome of corrosion products and facilitated Zn dissolution, leading to continuous pit growth.

A well-buffered local pH (7.05–7.38) was obtained at the interface of pure Zn in HBSS+Tris-HCl compared to that in HBSS (5.84–8.66). The corrosion rate of pure Zn decreased from 0.89 mm y^{-1} to 0.14 mm y^{-1} in the presence of Tris-HCl buffer. This was attributed to the strong buffering capability of Tris, binding the H^+ ions generated at the anodic sites caused by the hydrolysis of Zn^{2+} ions thus alleviating the acidification in the pit. The abated acidification decreased the accumulation of chlorides ions in the pit, inhibiting the pitting corrosion. Also, although Zn phosphates species maintained stable at this pH range (7.05–7.38) indicated by Hydra-Medusa in Fig. 6(a), the formation of Zn phosphates made little contribution to the protection of Zn substrate as supported by the slightly higher DO concentration detected at the interface of pure Zn in HBSS+Tris-HCl (2.8 ppm) compared to that in HBSS (2.5 ppm).

In HBSS+HEPES, local pH at the interface of pure Zn was further buffered at 7.19–7.45 compared to 7.05–7.38 in HBSS+Tris-HCl. The cathodic ORR slowed down as evidence by the minimum DO concentration: 3.4–3.8 ppm in HBSS+HEPES vs. 2.8–3.0 ppm in HBSS+Tris-HCl. This was because, besides the buffering capability, HEPES was also capable of strengthening the protection of the corrosion products layer formed on pure Zn [40], further blocking the diffusion of the oxygen from the electrolyte to the metal surface thus inhibiting ORR. This was also supported by the EIS spectra in Fig. 5, where a higher resistance at low frequency responsible for the corrosion resistant process of pure Zn was found within 1 h degradation of pure Zn in HBSS+HEPES compared to that in HBSS. A similar mechanism of diminishing ORR reaction has been recently shown for pure Mg [44]. As a consequence, the corrosion rate of pure Zn further decreased from 0.14 mm y $^{-1}$ in HBSS+Tris-HCl to 0.11 mm y $^{-1}$ in HBSS+HEPES. Note that typically, O₂ concentration

in bulk HBSS at 37 $^{\circ}\text{C}$ varies around 6 ppm.

The influence of Ca^{2+} ions on the degradation behavior of pure Zn was investigated in Ca^{2+} HBSS since Ca^{2+} ions have occupied a critical role during the degradation of Mg in SBF based on our previous studies [20,38]. A narrower range of local pH (6.84–7.68) was detected at the interface of pure Zn in Ca^{2+} HBSS compared to that in HBSS (5.84–8.66). The OH $^{-}$ anions generated by cathodic ORR were consumed by the formation of Ca-P-containing precipitates (as indicated by Hydra-Medusa in Fig. 6(b)), stabilizing local pH within the corresponding range. ORR slowed down as indicated by the higher DO concentration detected at the interface of pure Zn in Ca^{2+} HBSS (3.5–4.9 ppm) than that in HBSS (2.5–3.0 ppm), because the diffusion of oxygen was restricted by the Ca-P-containing products layer. As a result, the corrosion rate of pure Zn was remarkably lower (0.01 mm y $^{-1}$) in Ca^{2+} HBSS than that (0.89 mm y $^{-1}$) in HBSS. The similar pH-buffering capacity and barrier property of generating Ca-P-containing products were also reported for the degrading Fe-based alloys in Ca^{2+} HBSS [42].

Compared to the findings of degrading pure Zn in HBSS+Tris-HCl/HEPES, a similar performance of buffering local pH at the interface of pure Zn was exhibited in $\text{Ca}^{2+}\text{HBSS}$ buffered by Tris-HCl (7.28–7.42) or HEPES (7.27–7.44). However, the degradation of pure Zn was roughly ten-fold faster in $\text{Ca}^{2+}\text{HBSS}+\text{Tris-HCl/HEPES}$ (0.13 mm y^{-1}) compared to that in $\text{Ca}^{2+}\text{HBSS}$ (0.01 mm y^{-1}). The acceleration of the degradation rate was attributed to the effective pH buffering imposed by Tris that affects the formation of hydroxyls-containing corrosion products. Tris was also capable of binding Ca^{2+} ions, decreasing the concentration of the free Ca^{2+} ions in the electrolyte available for the formation of Ca-P precipitates [20]. Thus, the corrosion products layer formed at the interface of pure Zn in $\text{Ca}^{2+}\text{HBSS}+\text{Tris-HCl}$ became less protective than that in $\text{Ca}^{2+}\text{HBSS}$ (as supported by the disappearance of the partial overlap of two time constants in EIS spectra of pure Zn in $\text{Ca}^{2+}\text{HBSS}+\text{Tris-HCl}$ compared to that in $\text{Ca}^{2+}\text{HBSS}$ in Fig. 5). Local DO

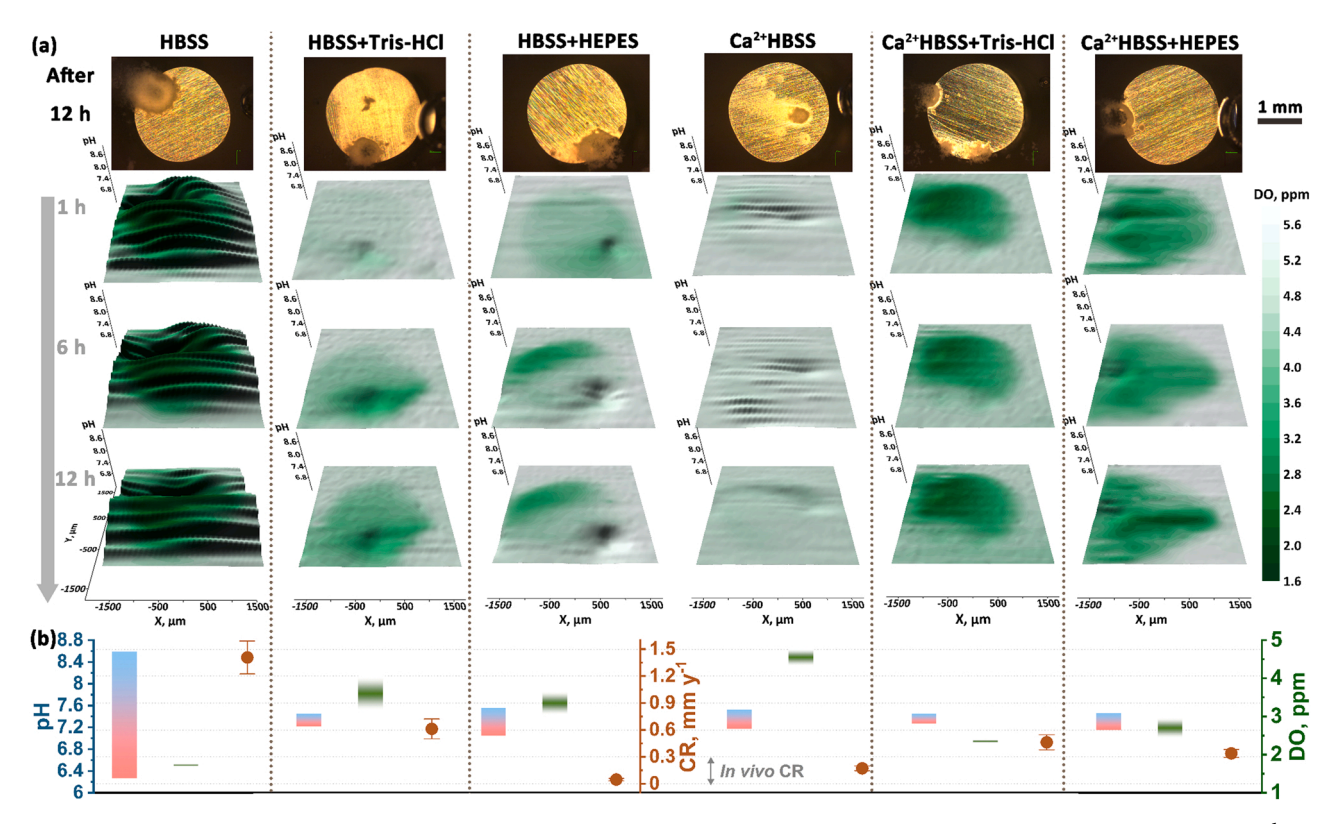


Fig. 4. The degradation behavior of Zn-0.8Ca in HBSS containing different pH buffers at 37 °C under hydrodynamic conditions (flow rate 1.0 mL min⁻¹). a visual appearances after 12 h of immersion, distribution of local pH (3D topography) and DO concentration (green color code) above the metal surface with immersion time. b a summary of local pH value (red-blue gradient), the range of minimum concentration of dissolved oxygen (green) and the corrosion rates, an average of three measurements (brown filled circles).

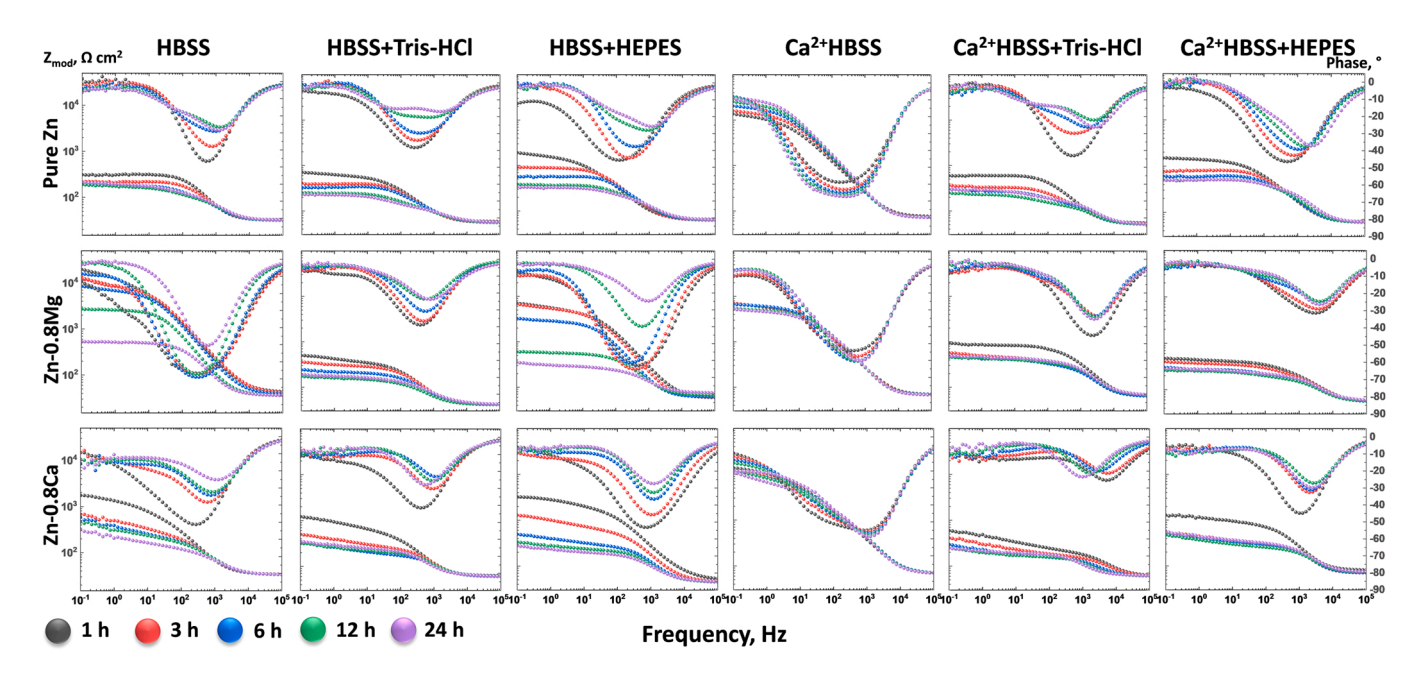


Fig. 5. The Bode plots of pure Zn, Zn-0.8Mg, and Zn-0.8Ca in HBSS containing different pH buffers at 37 °C during 24 h of immersion.

concentration at the interface of pure Zn decreased from 3.5 to 4.9 ppm in $\text{Ca}^{2+}\text{HBSS}$ to 3.0–4.5 ppm in $\text{Ca}^{2+}\text{HBSS+}\text{Tris-HCl}$ and 2.9–4.7 ppm in $\text{Ca}^{2+}\text{HBSS+}\text{HEPES}$. The slight decrease of DO concentration also suggested a diminished barrier property of the Ca-P-containing products layer against oxygen diffusion [42].

3.2. The degradation behavior of Zn-0.8Mg and Zn-0.8Ca in HBSS containing different pH buffers at 37 $^{\circ}$ C under hydrodynamic conditions

Similar experimental outcomes were also obtained for Zn-0.8Mg and Zn-0.8Ca alloys displayed in Figs. 3 and 4, respectively. Due to the alloying with more anodically active Mg and Ca, the corrosion rates of

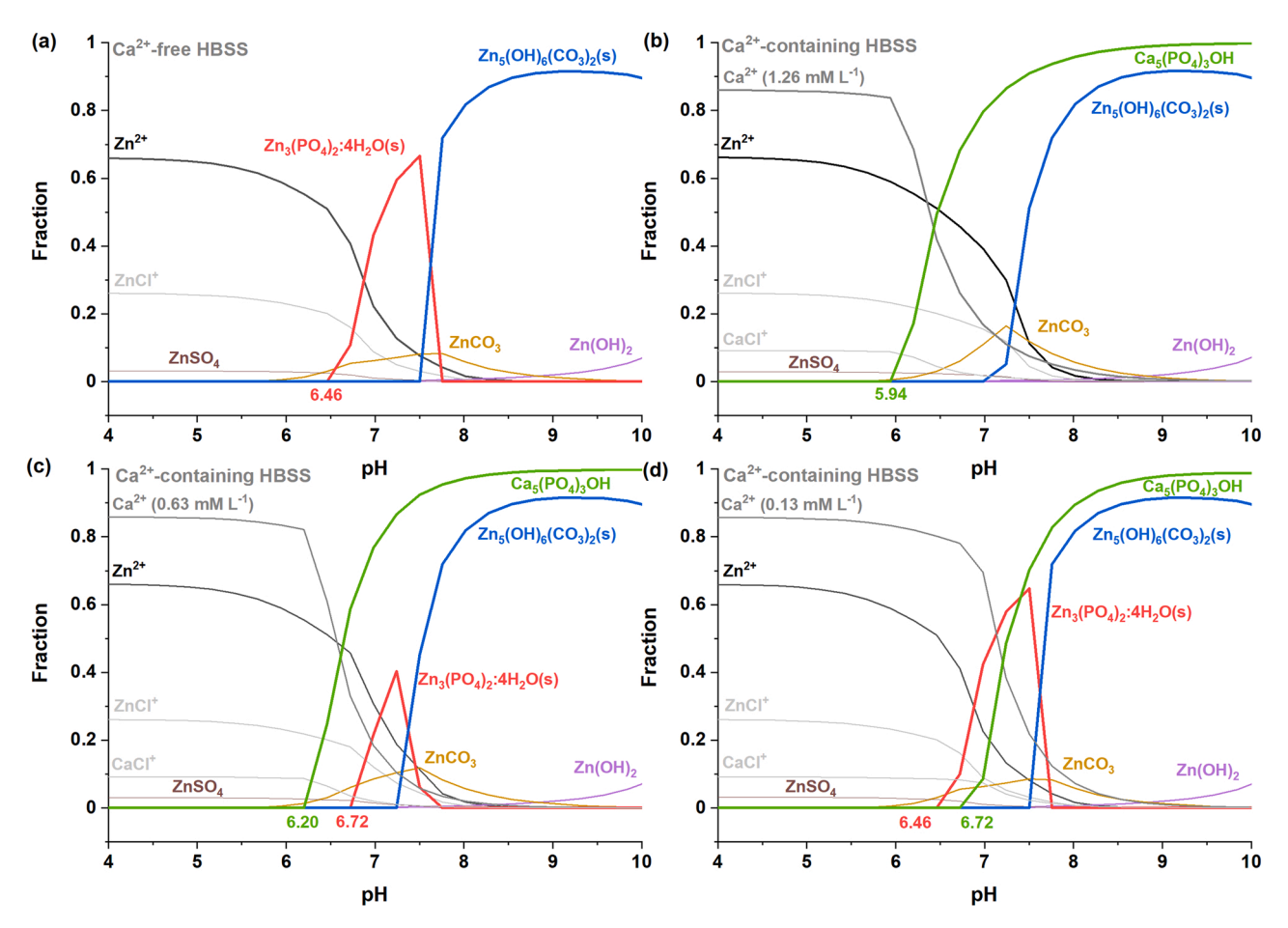


Fig. 6. The fraction of either Zn^{2+} or Ca^{2+} species as a function of pH in (a) Ca^{2+} -free HBSS and (b, c, d) Ca^{2+} -containing HBSS with different concentrations of Ca^{2+} ions, based on the thermodynamic stability constants simulated by Hydra-Medusa. The equilibrium concentrations of the participating species were taken equal to those listed in Table 1.

Zn alloys in HBSS increased from $0.89~\mathrm{mm~y}^{-1}$ (pure Zn) to $1.39~\mathrm{mm~y}^{-1}$ (Zn-0.8Mg), and $1.41~\mathrm{mm~y}^{-1}$ (Zn-0.8Ca). The range of local pH in HBSS above the surface of Zn-0.8Mg (6.32–9.08) and Zn-0.8Ca (6.27–8.59) was found different from that of pure Zn (5.84–8.66). The lowest value of local pH at anodic sites increased from 5.84 to 6.32 or 6.27, indicating a smaller amount of hydrolysis prone Zn²⁺ ions at anodic sites of Zn-0.8Mg or Zn-0.8Ca. The minimum DO concentration above the surface of Zn-0.8Mg (2.1–2.8 ppm) and Zn-0.8Ca (1.7–1.8 ppm) was lower than that for pure Zn (2.5–3.0 ppm), manifesting a higher rate of cathodic ORR especially on the surface of Zn-0.8Ca.

In HBSS+Tris-HCl, local pH was buffered at 7.45–7.85 for Zn-0.8Mg, and 7.22–7.45 for Zn-0.8Ca. DO consumption was inhibited (2.6–3.8 ppm for Zn-0.8Mg; 3.1–4.1 ppm for Zn-0.8Ca) and correlated to the lower corrosion rates (0.26 mm y $^{-1}$ for Zn-0.8Mg; 0.61 mm y $^{-1}$ for Zn-0.8Ca) compared to that in HBSS. A Strong corrosion inhibition was observed for Zn alloys in HBSS+HEPES, where local pH was controlled at 7.31–7.46 for Zn-0.8Mg and 7.05–7.56 for Zn-0.8Ca together with the higher oxygen concentration of 3.2–3.6 ppm (Zn-0.8Mg) and 3.0–3.7 (Zn-0.8Ca) than that in HBSS. The HEPES-facilitated protective layer blocked the $\rm O_2$ diffusion from the electrolyte to the alloy surface, accounting for their low corrosion rates (0.03 mm y $^{-1}$ for Zn-0.8Mg; 0.05 mm y $^{-1}$ for Zn-0.8Ca).

During the degradation of Zn-0.8Mg and Zn-0.8Ca in Ca²⁺HBSS, the precipitation of Ca-P-containing products involved the formation of corrosion products similar to that for pure Zn. The hydroxyls generated by cathodic ORR were consumed, which was supported by the decrease of local pH (from 9.08 to 7.88 for Zn-0.8Mg; from 8.59 to 7.53 for Zn-

0.8Ca). The involvement of Ca-P-containing products stabilized the corrosion products layer at the interface (as supported by the partial overlap of two time constants in the EIS spectra of Zn-0.8Mg and Zn-0.8Ca, which were similar to that of pure Zn in Fig. 5). Therefore, the strengthened corrosion products layer hindered the diffusion of the dissolved oxygen from electrolyte to the alloy surface (as indicated by the increased DO concentration (3.4-4.7 ppm for Zn-0.8Mg; 4.3-4.8 ppm for Zn-0.8Ca), and significantly reduced the corrosion rates to 0.31 mm y $^{-1}$ (Zn-0.8Mg) and 0.46 mm y $^{-1}$ (Zn-0.8Ca).

The contribution of Ca-P-containing products to strengthen the corrosion products layer on the surface of Zn-0.8Mg and Zn-0.8Ca was undermined by the addition of Tris-HCl or HEPES in the Ca²⁺HBSS (as also indicated by the disappearance of the overlay two time constants in the EIS spectra of Zn-0.8Mg and Zn-0.8Ca in Fig. 5). Because the strong pH buffering capacity of Tris or HEPES influenced the formation of hydroxyl-containing corrosion products. Tris and HEPES could also bind the free Ca²⁺ ions in the electrolyte available for the precipitation of Ca-P-containing products, notwithstanding local pH was well balanced at 7.13–7.51 (Zn-0.8Mg) or 7.27–7.45 (Zn-0.8Ca) in Ca²⁺HBSS+Tris-HCl, 7.23–7.43 (Zn-0.8Mg) or 7.15–7.46 (Zn-0.8Ca) Ca²⁺HBSS+HEPES. The barrier quality of the corrosion products layer weakened as presented by the decreased DO concentration at the interface of Zn-0.8Mg and Zn-0.8Ca in Ca²⁺HBSS+Tris-HCl (2.5-2.9 ppm for Zn-0.8Mg; 2.3-2.4 ppm for Zn-0.8Ca) and Ca²⁺HBSS+HEPES (2.6–3.7 ppm for Zn-0.8Mg; 2.4–3.0 ppm for Zn-0.8Ca). Thus, the corrosion rates of Zn-0.8Mg and Zn-0.8Ca are higher in $Ca^{2+}HBSS+Tris-HCl$ (0.31 mm y^{-1} for Zn-0.8Mg and 0.46 mm y^{-1} for Zn-0.8Ca) and $Ca^{2+}HBSS+HEPES$ (0.14 mm y^{-1} for Zn-0.8Mg and

 $0.34~\rm mm~y^{-1}$ for Zn-0.8Ca) compared to that in Ca²⁺HBSS (0.03 mm y^{-1} for Zn-0.8Mg and 0.05 mm y^{-1} for Zn-0.8Ca).

3.3. EIS analysis

Fig. 5 presents the Bode plots of pure Zn, Zn-0.8Mg, and Zn-0.8Ca acquired in different HBSS electrolytes at 37 °C during 24 h of immersion. The Bode plots obtained for degrading Zn-based alloys in HBSS showed that the contribution of ZnO to the corrosion resistance was correlated to the time constants at the frequency of 10³ Hz. In HBSS, the resistances detected at the low frequency related to the corrosion resistance of all three Zn-based alloys decreased with immersion time, and maintained generally lower than $10^3 \Omega \text{ cm}^2$. In contrast, in Ca²⁺HBSS, the resistances detected at the low frequency of all three Znbased alloys were significantly higher from the 1st hour of immersion, and generally further increased during 24 h of immersion remaining around $10^4 \Omega \text{ cm}^2$, which was roughly 10 times higher than that in HBSS. This was also consistent with the corrosion rates of Zn-based alloys in Fig. 7. A broad time constant appeared at the mid-frequency in the Bode plots of Zn-based alloys in Ca²⁺HBSS was a result of partial overlap of two time constants. The overlapped two time constants indicated that Ca-P-containing precipitates involved and stabilized the corrosion products layer at the interface of Zn-based alloys. This was different from the typical EIS spectra acquired on Mg in SBF, where an additional time constant emerged at the high frequency, correlating with the formation of Ca-P-containing products layer [20]. This additional time constant has been also found during the degradation of Fe-based alloys in Ca²⁺HBSS [45]. This difference could be probably attributed to the different properties of MgO and ZnO. Flawed MgO might be suitable for the growth of Ca-P-containing precipitates on the top, generating an extra products layer detected by EIS prior to MgO. By contrast, ZnO is more compact than MgO, and localized pitting corrosion is more characteristic of Zn than Mg. In this case, Ca-P-containing products would be inclined to grow at the interface rather than on the top. This is also supported by the characterization of the corrosion products layer on the surface of pure zinc during immersion in SBF [40, 46-48]. The resistance at low frequency kept increasing with the immersion time in Ca²⁺HBSS, and DO concentration increased from 2.5 to 3.0 ppm in HBSS to 3.5–4.9 ppm in Ca²⁺HBSS. This demonstrated that the involvement of Ca-P-containing products continuously reinforced the corrosion products layer at the interface, preventing oxygen access to Zn substrate, thus inhibiting cathodic ORR.

3.4. Summary and discussion

The influence of binding Ca²⁺ ions by Tris-HCl or HEPES on the formation of corrosion products during the degradation of Zn in Ca²⁺HBSS was also investigated by the simulation of Hydra-Medusa in HBSS electrolyte with different concentrations of Ca²⁺ ions (Fig. 6). The comprehensive studies on the characterization of the corrosion products during the corrosion of Zn and its alloys in Tris-HCl/HEPES buffered solutions have been reported in previous works [40,47,48]. In HBSS (Fig. 6(a)), corrosion products were mainly composed of Zn-P-containing products or zinc carbonates. In Ca²⁺HBSS (Fig. 6(b)), Ca-P-containing products were easier to generate than Zn-P-containing products if the concentration of Ca and P species was maintained.

Fig. 6(c) and 6(d) were constructed to consider the Ca²⁺-binding effect of Tris-HCl or HEPES. With the decrease of free Ca²⁺ ions, the pH related to the formation of Ca-P-containing products shifted right, indicating the precipitation could be inhibited to some extent. The remaining phosphate species could involve Zn²⁺ ions to generate Zn-P-containing products. Besides, the interfacial Zn-P-containing products have been recently found as the key to control the biocompatibility of Zn implants [49,50]. It is adverse to the formation of Zn-P-containing products if local pH is too high or too low (e.g. 5.84 or 8.66 during the degradation of pure Zn in HBSS) since the simulated pH range of forming zinc phosphates is 6.46–7.76 (Fig. 6(a)). This emphasizes the importance of controlling local pH during in vitro investigation of Zn alloys.

The ranges of local pH and DO concentration monitored during the degradation of all three types of Zn-based alloys in HBSS containing different buffers are summarized together with their corrosion rates in Fig. 7. In general, the addition of alloying elements (Mg, Ca) accelerated the degradation of Zn. This acceleration was accompanied by the enhanced cathodic ORR, which was supported by the stronger DO consumption on the surface of Zn-0.8Mg and Zn-0.8Ca compared to that

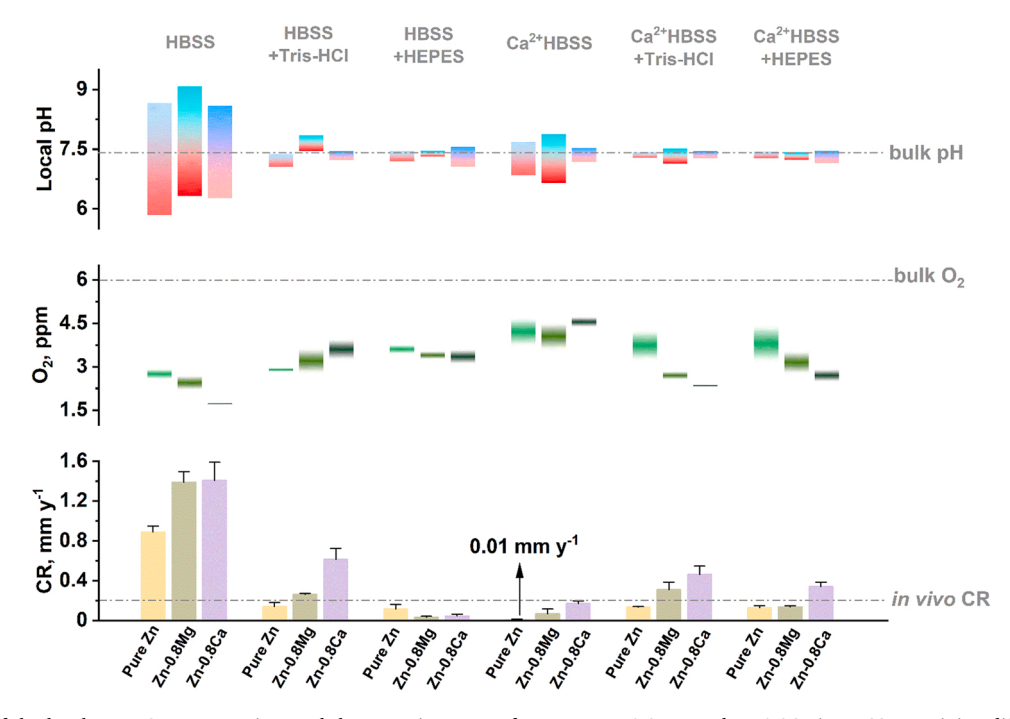


Fig. 7. A summary of the local pH, DO concentration, and the corrosion rates of pure Zn, Zn-0.8Mg, and Zn-0.8Ca in HBSS containing different buffers at 37 °C during 12 h of immersion under hydrodynamic conditions (The corrosion rates were measured after 3 days of immersion).

of pure Zn. Unlike Fe alloy where DO consumption also contributes to the oxidation of ferrous products to ferric compounds [42], oxygen concentration at the interface of Zn-based alloy mainly reflects the dynamics of cathodic ORR. Furthermore, it is worth mentioning that the oxygen concentration at the interface of Zn-based alloys could lower down to 1.7 ppm. It could be a plausible explanation for the inflammation around the implants of Zn alloys [51–53], because hypoxia has been reported to induce or aggravate inflammation [54]. The inflammation might differ depending on the Zn alloys and corresponding oxygen consumptions.

Despite a moderate fluctuation of local pH (6.7–7.9) at the interface of Zn alloys in $\text{Ca}^{2+}\text{HBSS}$ compared to that in HBSS (5.8–9.0), the value of local pH still exceeds the specific pH range for the purpose of simulating in vivo environment (e.g. 7.35–7.45 in the human plasma). The addition of Tris-HCl buffer in $\text{Ca}^{2+}\text{HBSS}$ could adjust the fluctuation of local pH and enable it to stabilize at a narrower pH range (7.1–7.5) compared to that (6.7–7.9) in $\text{Ca}^{2+}\text{HBSS}$. Given that HEPES reinforced the protective layer of corrosion products, an alternative degradation behavior would be likely to occur on Zn-based alloys in $\text{Ca}^{2+}\text{HBSS}+\text{HEPES}$, which might deviate from the simulation of in vivo environment.

The degradation process of Zn-based alloys in six HBSS electrolytes containing different buffers was summarized in Fig. 8 based on the results in this work and the data reported in previous studies [6,40]. In ${\rm Ca}^{2+}{\rm HBSS}$, the precipitation of Ca-P-containing products consumed the phosphate species in the electrolyte, suppressing the formation of Zn-P-containing products (as supported by Fig. 6(b)). Under the premise of buffering local pH, the ${\rm Ca}^{2+}$ -binding ability of Tris-HCl reduced the consumption of phosphates by ${\rm Ca}^{2+}$ ions, enabling the formation of Zn-P-containing products and postponing the precipitation of Ca-P-containing products (as indicated in Fig. 6(c, d)).

Furthermore, unlike the generally slower in vivo degradation of biodegradable Mg alloys compared to in vitro [55], in vivo degradation rate of Zn alloys varies at different locations (avg. $0.02~\text{mm y}^{-1}$ for vascular stent applications [3], avg. $0.15~\text{mm y}^{-1}$ for load-bearing applications [6]). The corrosion rates of Zn alloys in Ca²⁺HBSS (avg. $0.08~\text{mm y}^{-1}$) are close to in vivo degradation rate of Zn alloys for vascular stent applications, while the corrosion rates of Zn alloys in Ca²⁺HBSS+Tris-HCl/HEPES ($0.13-0.46~\text{mm y}^{-1}$) are close to the in vivo degradation rate of Zn alloys for load-bearing applications. This discrepancy can be attributed to the different in vivo environment around Zn implants. Further efforts should be spent on studying the effect of other factors (e.g. amino acids, proteins, stress/strain et al.) on the degradation of Zn alloys. Recently, Tris-HCl buffered amino acids/glucose-containing SBF has been found as a recommended option

for the replication and prediction of in vivo biodegradation of zinc [23]. Also, during the degradation of Mg in proteins-containing HBSS, bovine serum albumin (BSA) has been found to have the capacity of Ca^{2+} ions chelation and pH buffering [24], which was similar to the role of Tris-HCl on the degradation of Zn-based alloys in Ca^{2+} HBSS. The chelation of BSA and Zn^{2+} ions has also been reported to increase the corrosion rate of pure Zn in artificial plasma [25]. The influence of proteins and amino acids on the variation of local pH and oxygen concentration at the interface of biodegradable Zn-based alloys would be explored in future studies.

In addition, a tiny amount of dissolved H_2 (0.5–1.5 μ mol L^{-1}) was detected at the interface of degrading Zn alloys in Ca^{2+} HBSS (Fig. 9), verifying that ORR is the major cathodic reaction during the degradation of Zn alloys in HBSS. However, it should be pointed out that hydrogen evolution mainly happened in the pits, where the pH slightly decreased. The growth of the corrosion products layer could also block oxygen diffusion, enabling the hydrogen evolution reaction to gradually take place and produce hydrogen.

4. Conclusion

Local interface pH during corrosion of pure Zn, Zn-0.8Mg, and Zn-0.8Ca alloys varied in the wide range of 5.8 – 9.0 in HBSS and slightly narrow range of 6.7 – 7.9 in Ca $^{2+}$ HBSS. The addition of synthetic pH buffers, either Tris-HCl or HEPES, stabilized local pH at 7.4 \pm 0.2 at the interface of degrading Zn-based alloys in HBSS (pH=7.4) at 37 $^{\circ}$ C under hydrodynamic conditions. This differs from the effect of Tris-HCl and HEPES on Mg substrate where local pH could not be buffered. Although both Tris-HCl or HEPES could balance the local pH at Zn interface, HEPES could also enhance the growth of products layer which might change the degradation behavior of Zn alloys.

Local concentration of dissolved oxygen at the interface of Zn-based alloys reached 2.3 ppm in Ca^{2+} HBSS and as low as 1.7 ppm in Ca^{2+} deficient HBSS. This is only ca. 40% and 30% correspondingly of the level of dissolved oxygen in bulk electrolytes. Significant depletion of the level of dissolved oxygen in the vicinity of Zn and alloys offers a possible explanation for the inflammation around Zn implants in vivo. A low rate hydrogen evolution reaction was detected in pits with the amount of dissolved H_2 reaching only 0.5–1.5 µmol L^{-1} .

The corrosion rate of Zn alloyed with 0.8 wt%Mg or 0.8 wt%Ca was consistently higher compared to that of pure Zn in all tested media, namely ${\rm Ca^{2^+}}$ -containing and ${\rm Ca^{2^+}}$ -deficient HBSS with or without synthetic pH buffers. For pure Zn, CR varied from 0.01 to 0.89 mm ${\rm y^{-1}}$ depending on the medium, while for two alloys, the corrosion rate varied in the range between 0.14 and 0.31 mm ${\rm y^{-1}}$ for Zn-0.8Mg and

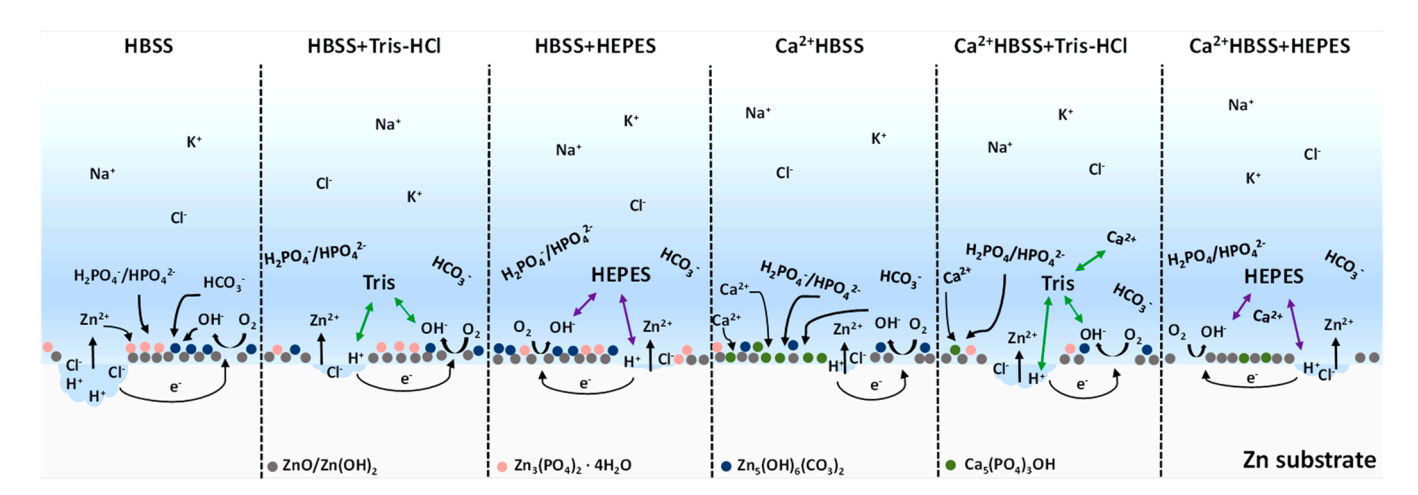


Fig. 8. A schematic illustration of the degradation process of Zn-based alloys in six HBSS electrolytes (The corrosion products indicated in the diagram is based on the simulation of Hydra-Medusa (Fig. 6) and previous work [40]).

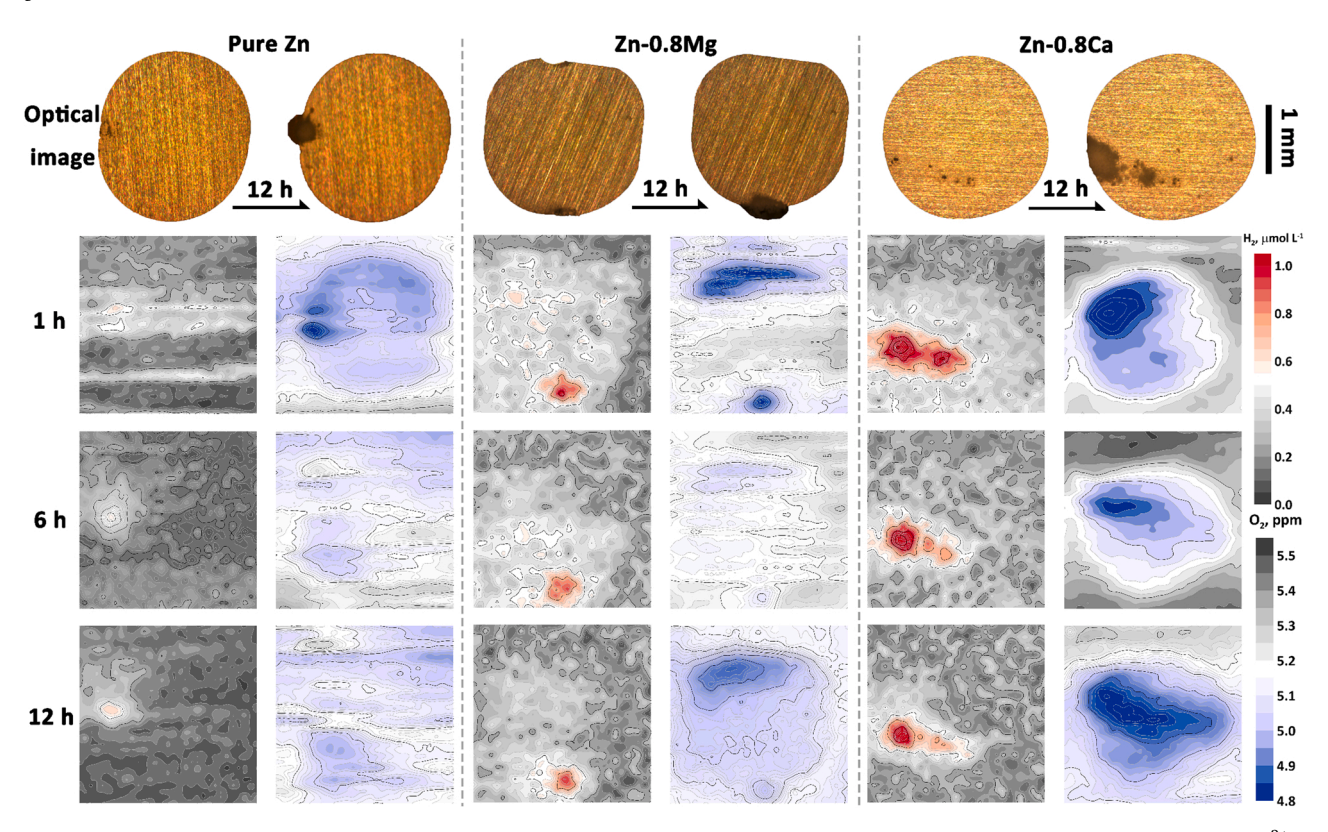


Fig. 9. The visual appearances, and the distribution of local dissolved H_2 and O_2 concentration of pure Zn and Zn alloys during 12 h of immersion in Ca^{2+} HBSS at 37 °C under hydrodynamic conditions (flow rate: 1.0 mL min⁻¹).

 $0.34-0.46\ mm\ y^{-1}$ for Zn-0.8Ca in Tris-HCl and HEPES buffered $\text{Ca}^{2+}\text{HBSS}$ electrolytes.

Considering the values of local pH and corrosion rate compared to physiological conditions, both Tris-HCl and HEPES buffered $\text{Ca}^{2+}\text{HBSS}$ electrolytes can be recommended for corrosion and in vitro studies of Zn-based alloys.

CRediT author contribution statement

Cheng Wang: Conceptualization, Methodology, Validation, Formal analysis, Investigation, Data curation, Writing – original draft, Writing – review & editing, Visualization. Xiao Liu: Investigation, Writing – review & editing. Di Mei: Investigation, Writing – review & editing. Min Deng: Investigation, Writing – review & editing. Yufeng Zheng: Conceptualization, Resources, Writing – review & editing, Supervision, Project administration, Funding acquisition. Mikhail L. Zheludkevich: Conceptualization, Supervision, Writing – review & editing. Sviatlana V. Lamaka: Conceptualization, Resources, Supervision, Writing – review & editing.

Declaration of Competing Interest

The authors declare that they have no known competing financial interests or personal relationships that could have appeared to influence the work reported in this paper.

Data availability

The raw/processed data required to reproduce these findings cannot be shared at this time as the data also forms part of an ongoing study.

Acknowledgment

Mr. Cheng Wang thanks the China Scholarship Council for the award

of fellowship and funding (No. 201806310128). Dr. Yufeng Zheng thanks the support of key project, National Natural Science Foundation of China (Grant No. 51931001). The authors genuinely appreciate Dr. Dawei Zhang from University of Science and Technology Beijing for kindly contributing to this cooperation. The technical support of Mr. Volker Heitmann and Mr. Ulrich Burmester during this work is gratefully acknowledged.

References

- Y.F. Zheng, X.N. Gu, F. Witte, Biodegradable metals, Mater. Sci. Eng. R Rep. 77 (2014) 1–34.
- [2] P.K. Bowen, J. Drelich, J. Goldman, Zinc exhibits ideal physiological corrosion behavior for bioabsorbable stents, Adv. Mater. 25 (2013) 2577–2582.
- [3] E. Mostaed, M. Sikora-Jasinska, J.W. Drelich, M. Vedani, Zinc-based alloys for degradable vascular stent applications, Acta Biomater. 71 (2018) 1–23.
- [4] X. Tong, W. Cai, J. Lin, K. Wang, L. Jin, Z. Shi, D. Zhang, J. Lin, Y. Li, M. Dargusch, C. Wen, Biodegradable Zn-3Mg-0.7Mg2Si composite fabricated by high-pressure solidification for bone implant applications, Acta Biomater. 123 (2021) 407-417.
- [5] P.K. Bowen, R.J. Guillory 2nd, E.R. Shearier, J.M. Seitz, J. Drelich, M. Bocks, F. Zhao, J. Goldman, Metallic zinc exhibits optimal biocompatibility for bioabsorbable endovascular stents, Mater. Sci. Eng. C Mater. Biol. Appl. 56 (2015) 467–472.
- [6] H. Yang, B. Jia, Z. Zhang, X. Qu, G. Li, W. Lin, D. Zhu, K. Dai, Y. Zheng, Alloying design of biodegradable zinc as promising bone implants for load-bearing applications, Nat. Commun. 11 (2020) 401.
- [7] J. Venezuela, M.S. Dargusch, The influence of alloying and fabrication techniques on the mechanical properties, biodegradability and biocompatibility of zinc: a comprehensive review. Acta Biomater. 87 (2019) 1–40.
- [8] X. Tong, D. Zhang, X. Zhang, Y. Su, Z. Shi, K. Wang, J. Lin, Y. Li, J. Lin, C. Wen, Microstructure, mechanical properties, biocompatibility, and in vitro corrosion and degradation behavior of a new Zn-5Ge alloy for biodegradable implant materials, Acta Biomater. 82 (2018) 197–204.
- [9] J. Lin, X. Tong, Z. Shi, D. Zhang, L. Zhang, K. Wang, A. Wei, L. Jin, J. Lin, Y. Li, C. Wen, A biodegradable Zn-1Cu-0.1Ti alloy with antibacterial properties for orthopedic applications, Acta Biomater. 106 (2020) 410–427.
- [10] A.J. Drelich, S. Zhao, R.J. Guillory 2nd, J.W. Drelich, J. Goldman, Long-term surveillance of zinc implant in murine artery: Surprisingly steady biocorrosion rate, Acta Biomater. 58 (2017) 539–549.
- [11] H. Yang, C. Wang, C. Liu, H. Chen, Y. Wu, J. Han, Z. Jia, W. Lin, D. Zhang, W. Li, W. Yuan, H. Guo, H. Li, G. Yang, D. Kong, D. Zhu, K. Takashima, L. Ruan, J. Nie,

- X. Li, Y. Zheng, Evolution of the degradation mechanism of pure zinc stent in the one-year study of rabbit abdominal aorta model, Biomaterials 145 (2017) 92–105.
- [12] R.J. Guillory 2nd, M. Sikora-Jasinska, J.W. Drelich, J. Goldman, In vitro corrosion and in vivo response to zinc implants with electropolished and anodized surfaces, ACS Appl. Mater. Interfaces (2019).
- [13] D. Zhu, I. Cockerill, Y. Su, Z. Zhang, J. Fu, K.W. Lee, J. Ma, C. Okpokwasili, L. Tang, Y. Zheng, Y.X. Qin, Y. Wang, Mechanical strength, biodegradation, and in vitro and in vivo biocompatibility of Zn biomaterials, ACS Appl. Mater. Interfaces 11 (2019) 6809–6819.
- [14] Y. Sheng, J. Yang, X. Zhao, H. Liu, S. Cui, L. Chen, R. Zeng, X. Wang, C.H. Huang, W. Li, Development and in vitro biodegradation of biomimetic zwitterionic phosphorylcholine chitosan coating on Zn1Mg alloy, ACS Appl. Mater. Interfaces 12 (2020) 54445–54458.
- [15] Y. Meng, L. Liu, D. Zhang, C. Dong, Y. Yan, A.A. Volinsky, L.N. Wang, Initial formation of corrosion products on pure zinc in saline solution, Bioact. Mater. 4 (2019) 87–96.
- [16] K. Torne, M. Larsson, A. Norlin, J. Weissenrieder, Degradation of zinc in saline solutions, plasma, and whole blood, J. Biomed. Mater. Res B Appl. Biomater. 104 (2016) 1141–1151.
- [17] Y. Chen, W. Zhang, M.F. Maitz, M. Chen, H. Zhang, J. Mao, Y. Zhao, N. Huang, G. Wan, Comparative corrosion behavior of Zn with Fe and Mg in the course of immersion degradation in phosphate buffered saline, Corros. Sci. 111 (2016) 541–555
- [18] H. Guo, R.H. Cao, Y.F. Zheng, J. Bai, F. Xue, C.L. Chu, Diameter-dependent in vitro performance of biodegradable pure zinc wires for suture application, J. Mater. Sci. Technol. 35 (2019) 1662–1670.
- [19] L. Liu, Y. Meng, C. Dong, Y. Yan, A.A. Volinsky, L.-N. Wang, Initial formation of corrosion products on pure zinc in simulated body fluid, J. Mater. Sci. Technol. 34 (2018) 2271–2282.
- [20] D. Mei, S.V. Lamaka, J. Gonzalez, F. Feyerabend, R. Willumeit-Römer, M. L. Zheludkevich, The role of individual components of simulated body fluid on the corrosion behavior of commercially pure Mg, Corros. Sci. 147 (2019) 81–93.
- [21] D. Mei, C. Wang, M. Nienaber, M. Pacheco, A. Barros, S. Neves, R.L. Reis, S. Zhu, J. Bohlen, D. Letzig, S. Guan, M.L. Zheludkevich, S.V. Lamaka, Corrosion behavior of Mg wires for ureteral stent in artificial urine solution, Corros. Sci. 189 (2021).
- [22] D. Mei, S.V. Lamaka, C. Feiler, M.L. Zheludkevich, The effect of small-molecule bio-relevant organic components at low concentration on the corrosion of commercially pure Mg and Mg-0.8Ca alloy: an overall perspective, Corros. Sci. 153 (2019) 258–271.
- [23] X. Liu, Y. Cheng, Z. Guan, Y. Zheng, Exploring the effect of amino acid and glucose on the biodegradation of pure Zn, Corros. Sci. 170 (2020).
- [24] D. Mei, C. Wang, S.V. Lamaka, M.L. Zheludkevich, Clarifying the influence of albumin on the initial stages of magnesium corrosion in Hank's balanced salt solution, J. Magnes. Alloy. (2020).
- [25] L. Liu, Y. Meng, A.A. Volinsky, H.-J. Zhang, L.-N. Wang, Influences of albumin on in vitro corrosion of pure Zn in artificial plasma, Corros. Sci. 153 (2019) 341–356.
- [26] D. Zhu, Y. Su, M.L. Young, J. Ma, Y. Zheng, L. Tang, Biological responses and mechanisms of human bone marrow mesenchymal stem cells to Zn and Mg biomaterials, ACS Appl. Mater. Interfaces 9 (2017) 27453–27461.
- [27] C.M.H. Ferreira, I.S.S. Pinto, E.V. Soares, H.M.V.M. Soares, (Un)suitability of the use of pH buffers in biological, biochemical and environmental studies and their interaction with metal ions – a review, RSC Adv. 5 (2015) 30989–31003.
- [28] S. Lamaka, R.M. Souto, M.G.S. Ferreira, In-situ visualization of local corrosion by Scanning Ion-selective Electrode Technique (SIET), Microsc. Sci. Technol. Appl. Educ (2010) 2162–2173
- [29] T. Kokubo, H. Takadama, How useful is SBF in predicting in vivo bone bioactivity? Biomaterials 27 (2006) 2907–2915.
- [30] M. Schinhammer, J. Hofstetter, C. Wegmann, F. Moszner, J.F. Löffler, P. J. Uggowitzer, On the immersion testing of degradable implant materials in simulated body fluid: active pH regulation using CO₂, Adv. Eng. Mater. 15 (2013) 434–441.
- [31] J. Walker, S. Shadanbaz, N.T. Kirkland, E. Stace, T. Woodfield, M.P. Staiger, G. J. Dias, Magnesium alloys: predicting in vivo corrosion with in vitro immersion testing, J. Biomed. Mater. Res. B Appl. Biomater. 100 (2012) 1134–1141.
- [32] N.I. Zainal Abidin, B. Rolfe, H. Owen, J. Malisano, D. Martin, J. Hofstetter, P. J. Uggowitzer, A. Atrens, The in vivo and in vitro corrosion of high-purity magnesium and magnesium alloys WZ21 and AZ91, Corros. Sci. 75 (2013) 354–366.
- [33] M.A. Metrick, J.E. Temple, G. MacDonald, The effects of buffers and pH on the thermal stability, unfolding and substrate binding of RecA, Biophys. Chem. 184 (2013) 29–36.

- [34] Z. Darzynkiewicz, B. Jacobson, HEPES-buffered media in lymphocyte cultures, Proc. Soc. Exp. Biol. Med. 136 (1971) 387–393.
- [35] Y. Xin, P.K. Chu, Influence of Tris in simulated body fluid on degradation behavior of pure magnesium, Mater. Chem. Phys. 124 (2010) 33–35.
- [36] S. Naddaf Dezfuli, Z. Huan, J.M.C. Mol, M.A. Leeflang, J. Chang, J. Zhou, Influence of HEPES buffer on the local pH and formation of surface layer during in vitro degradation tests of magnesium in DMEM, Prog. Nat. Sci. Mater. Int. 24 (2014) 531–538.
- [37] S.S. Jamali, S.E. Moulton, D.E. Tallman, M. Forsyth, J. Weber, G.G. Wallace, Applications of scanning electrochemical microscopy (SECM) for local characterization of AZ31 surface during corrosion in a buffered media, Corros. Sci. 86 (2014) 93–100.
- [38] S.V. Lamaka, J. Gonzalez, D. Mei, F. Feyerabend, R. Willumeit-Römer, M. L. Zheludkevich, Local pH and its evolution near mg alloy surfaces exposed to simulated body fluids, Adv. Mater. Interfaces 5 (2018), 1800169.
- [39] M.B. Kannan, H. Khakbaz, A. Yamamoto, Understanding the influence of HEPES buffer concentration on the biodegradation of pure magnesium: an electrochemical study, Mater. Chem. Phys. 197 (2017) 47–56.
- [40] X. Liu, H. Yang, P. Xiong, W. Li, H.-H. Huang, Y. Zheng, Comparative studies of Tris-HCl, HEPES and NaHCO3/CO₂ buffer systems on the biodegradation behaviour of pure Zn in NaCl and SBF solutions, Corros. Sci. (2019).
- [41] D. Mei, S.V. Lamaka, X. Lu, M.L. Zheludkevich, Selecting medium for corrosion testing of bioabsorbable magnesium and other metals – a critical review, Corros. Sci. 171 (2020), 108722.
- [42] C. Wang, C. Tonna, D. Mei, J. Buhagiar, M.L. Zheludkevich, S.V. Lamaka, Biodegradation behaviour of Fe-based alloys in Hanks' Balanced Salt Solutions: Part II. The evolution of local pH and dissolved oxygen concentration at metal interface, Bioact. Mater. 7 (2022) 412–425.
- [43] G.S. Dr. James. Lange's Handbook of Chemistry, Seventeenth Edition, 17th edition ed., McGraw-Hill Education, New York, 2017.
- [44] C. Wang, D. Mei, G. Wiese, L. Wang, M. Deng, S.V. Lamaka, M.L. Zheludkevich, High rate oxygen reduction reaction during corrosion of ultra-high-purity magnesium, npj Mater. Degrad. 4 (2020).
- [45] C. Tonna, C. Wang, D. Mei, S.V. Lamaka, M.L. Zheludkevich, J. Buhagiar, Biodegradation behaviour of Fe-based alloys in Hanks' Balanced Salt Solutions: Part I. material characterisation and corrosion testing, Bioact. Mater. 7 (2022) 426–440.
- [46] S. Huang, W. Wu, Y. Su, L. Qiao, Y. Yan, Insight into the corrosion behaviour and degradation mechanism of pure zinc in simulated body fluid, Corros. Sci. 178 (2021).
- [47] H. Dong, F. Lin, A.R. Boccaccini, S. Virtanen, Corrosion behavior of biodegradable metals in two different simulated physiological solutions: comparison of Mg, Zn and Fe, Corros. Sci. 182 (2021).
- [48] X. Liu, H. Yang, Y. Liu, P. Xiong, H. Guo, H.-H. Huang, Y. Zheng, Comparative studies on degradation behavior of pure zinc in various simulated body fluids, Jom 71 (2019) 1414–1425.
- [49] Y. Su, H. Yang, J. Gao, Y.X. Qin, Y. Zheng, D. Zhu, Interfacial zinc phosphate is the key to controlling biocompatibility of metallic zinc implants, Adv. Sci. (2019), 1900112.
- [50] L. Zhang, X. Tong, J. Lin, Y. Li, C. Wen, Enhanced corrosion resistance via phosphate conversion coating on pure Zn for medical applications, Corros. Sci. 169 (2020), 108602.
- [51] R.J. Guillory 2nd, P.K. Bowen, S.P. Hopkins, E.R. Shearier, E.J. Earley, A. A. Gillette, E. Aghion, M. Bocks, J.W. Drelich, J. Goldman, Corrosion characteristics dictate the long-term inflammatory profile of degradable zinc arterial implants, ACS Biomater. Sci. Eng. 2 (2016) 2355–2364.
- [52] X. Liu, W. Yuan, D. Shen, Y. Cheng, D. Chen, Y. Zheng, Exploring the biodegradation of pure Zn under simulated inflammatory condition, Corros. Sci. 189 (2021), 109606.
- [53] G. Bao, Q. Fan, D. Ge, K. Wang, M. Sun, Z. Zhang, H. Guo, H. Yang, B. He, Y. Zheng, In vitro and in vivo studies to evaluate the feasibility of Zn-0.1Li and Zn-0.8Mg application in the uterine cavity microenvironment compared to pure zinc, Acta Biomater. 123 (2021) 393–406.
- [54] H.K. Eltzschig, P. Carmeliet, Hypoxia and inflammation, N. Engl. J. Med 364 (2011) 656–665.
- [55] A.H. Martinez Sanchez, B.J. Luthringer, F. Feyerabend, R. Willumeit, Mg and Mg alloys: how comparable are in vitro and in vivo corrosion rates? A review, Acta Biomater. 13 (2015) 16–31.